Ultramicroscopy 248 (2023) 113705

Contents lists available at ScienceDirect

Ultramicroscopy

journal homepage: www.elsevier.com/locate/ultramic

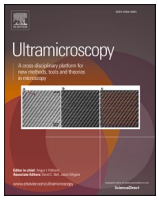

An iterative method for reference pattern selection in high-resolution electron backscatter diffraction (HR-EBSD)

Abdalrhaman Koko [*,a,b], Vivian Tong [b], Angus J. Wilkinson [a], T. James Marrow [a]

[a] Department of Materials, University of Oxford, Oxford OX1 3PH, United Kingdom
[b] National Physical Laboratory, Hampton Road, Teddington TW11 0LW, United Kingdom

ARTICLE INFO

Keywords:
HR-EBSD
Strain measurement
EBSD
Electron microscopy

ABSTRACT

For high (angular) resolution electron backscatter diffraction (HR-EBSD), the selection of a reference diffraction pattern ($EBSP_0$) significantly affects the precision of the calculated strain and rotation maps. This effect was demonstrated in plastically deformed body-centred cubic and face-centred cubic ductile metals (ferrite and austenite grains in duplex stainless steel) and brittle single-crystal silicon, which showed that the effect is not only limited to measurement magnitude but also spatial distribution. An empirical relationship was then identified between the cross-correlation parameter and angular error, which was used in an iterative algorithm to identify the optimal reference pattern that maximises the precision of HR-EBSD.

1. Introduction

Electron backscatter diffraction (EBSD) technique offers an impressive combination of sensitivity, spatial resolution and ease of use compared to other methods in measuring the elastic strains and estimating the geometrically necessary dislocation (GND) density which provides quantitative information about a material's elastic and plastic behavior at the microscale [1–3]. For electron backscatter diffraction microscopy, a flat polished crystalline specimen is placed inside a scanning electron microscope (SEM) [4]. Tilting the sample elongates the interaction volume perpendicular to the tilt axis, allowing more backscattered electrons to leave the sample [5,6]. The electron beam (typically 20 kV) is focused on a small volume and backscatters at a spatial resolution of ~20 nm at the specimen surface [7]. The spatial resolution varies with angular width [8], interaction volume [9], and nature of the material under study [7] (in the related technique of transmission Kikuchi diffraction, the resolution also varies with the specimen thickness [10]. Thus, increasing the beam energy increases the interaction volume and decreases the spatial resolution [11].

Rastering the beam position to obtain EBSD maps can provide information about texture, grain size, misorientation across boundaries (e.g., grain or twin), and local misorientations of the crystal [1,12,13]. In addition, finer features (e.g., phase, polarity) can be adequately quantified from the intensity distribution within the Kikuchi bands [14]. Furthermore, the change and degradation in electron backscatter patterns (EBSPs) provide information about the diffracting volume. Pattern degradation (i.e., diffuse quality) can be used to assess the level of plasticity through the pattern or image quality (IQ) [15], where IQ is calculated from the sum of the peaks detected when using the conventional Hough transform [16]. Wilkinson [17] first used the changes in high-order Kikuchi line positions to determine elastic strains, albeit with low precision[1] (0.3% to 1%); however, this approach cannot be used for characterising residual elastic strain in metals as the elastic strain at the yield point is usually around 0.2%. Measuring strain by tracking the change in the higher-order Kikuchi lines is practical when the strain is small, as the band position is sensitive to changes in lattice parameters [18]. In the early 1990s, Troost et al. [19] and Wilkinson and Dingley [20,21] used pattern degradation and change in the zone axis position to measure the residual elastic deviatoric strains and small lattice rotations with a 0.02% precision.

Cross-correlation-based, high angular resolution electron backscatter diffraction (HR-EBSD) – introduced by Wilkinson et al. [22,23] –

* Corresponding author at: Department of Materials, University of Oxford, Oxford OX1 3PH, United Kingdom.
E-mail address: abdo.koko@materials.ox.ac.uk (A. Koko).

[1] Throughout the paper, the terms 'error', and 'precision' were used as defined in International Bureau of Weights and Measures (BIPM) guide to measurement uncertainty (GUM). The true value in any measurement is in practice unknowable, therefore treat 'error', 'accuracy', and 'uncertainty' as synonymous, and 'true value' and 'best guess' as synonymous. Precision is the variance (or standard deviation) between all estimated quantities. Bias is the difference between average of measured values and an independently measured 'best guess'. Accuracy is then the combination of bias and precision.

https://doi.org/10.1016/j.ultramic.2023.113705
Received 12 June 2022; Received in revised form 15 January 2023; Accepted 17 February 2023
Available online 20 February 2023

is a scanning electron microscopy (SEM) -based technique to map relative deviatoric elastic strains and rotations, and estimate the geometrically necessary dislocation (GND) density in crystalline materials. HR-EBSD method uses image cross-correlation to measure pattern shifts between regions of interest (ROI) between electron backscatter diffraction patterns (EBSPs) with sub-pixel precision. As a result, the relative lattice distortion between two points in a crystal can be calculated using pattern shifts from at least four non-collinear ROI. In practice, pattern shifts are measured in more than 20 ROI per EBSP to find a best-fit solution to the deformation gradient tensor, representing the relative lattice distortion[2] [22–25]. However, these measurements do not provide information about the volumetric/hydrostatic strains. Full details of the HR-EBSD method are given in [24,26].

Elastic strain and (elastic) lattice rotation tensors are calculated by decomposing the deformation gradient tensor into symmetric and anti-symmetric parts, respectively. Non-hydrostatic components of the residual stress are determined from the elastic strain tensor using Hooke's law with anisotropic elastic stiffness constants. The hydrostatic elastic strain component can also be estimated by assuming that the stress normal to the surface (σ_{33}) is zero (i.e., a traction-free surface [23,27]). Furthermore, the geometrically necessary dislocation (GND) density can be estimated from the HR-EBSD measured lattice rotations by relating the rotation axis and angle between neighbour map points to the dislocation types and densities in a material using Nye's tensor [28,29].

The HR-EBSD method was shown [23,30–32] to achieve a precision of $\pm 10^{-4}$ in components of the displacement gradient tensors (i.e., strain and rotation in radians) by measuring the shifts at a pattern image resolution of ± 0.05 pixels. Still, it was limited to small strains and rotations ($>1.5^{\circ}$). Britton and Wilkinson [24] raised the rotation limit to $\approx 11^{\circ}$ by using a re-mapping technique [33] that recalculated the strain after transforming the patterns with a rotation matrix calculated from the 1st cross-correlation iteration. However, further lattice rotation, typically caused by severe plastic deformation, will cause errors in the elastic strain calculations. Ruggles et al. [34] demonstrated an improved HR-EBSD precision, even at 12° of lattice rotation, using the inverse compositional Gauss–Newton-based (ICGN) method instead of cross-correlation. Vermeij and Hoefnagels [35] also established a method that achieves a precision of $\pm 10^{-5}$ in the displacement gradient components using a full-field integrated digital image correlation (IDIC) framework instead of dividing the EBSPs into small ROIs. Patterns in IDIC are distortion-corrected to negate the need for re-mapping up to $\approx 14^{\circ}$ [36,37].

Nonetheless, in HR-EBSD analysis, the lattice distortion field is still calculated relative to a reference pattern or point ($EBSP_0$) per grain in the map, and is dependent on the lattice distortion at the point. The lattice distortion field in each grain is measured with respect to this point; therefore, the absolute lattice distortion at the reference point (relative to the unstrained crystal) is excluded from the HR-EBSD elastic strain and rotation maps [38–40]. This 'reference pattern problem' is similar to the 'd_0 problem' in X-ray diffraction [41,42], and affects the nominal magnitude of HR-EBSD stress fields. However, selecting the reference pattern ($EBSP_0$) plays a key role, as severely deformed $EBSP_0$ adds phantom lattice distortions to the map values, thus, decreasing the measurement precision [38,39].

The use of simulated reference patterns for absolute strain measurement is still an active area of research [14,43–50] and scrutiny [38, 50–55] as difficulties arise from a variation of inelastic electron scattering with depth which limits the accuracy of dynamical diffraction simulation models, and imprecise determination of the pattern centre which leads to phantom strain components which cancel out when using experimentally acquired reference patterns. Other methods assumed that absolute strain at $EBSP_0$ can be determined using crystal plasticity finite-element (CPFE) simulations, which then can be then combined with the HR-EBSD data (e.g., using linear 'top-up' method [56,57] or displacement integration [58]) to calculate the absolute lattice distortions.

In addition, GND density estimation is nominally insensitive to (or negligibly dependent upon [59,60]) $EBSP_0$ choice, as only neighbour point-to-point differences in the lattice rotation maps are used for GND density calculation [61,62]. However, this assumes that the absolute lattice distortion of $EBSP_0$ only changes the relative lattice rotation map components by a constant value which vanishes during derivative operations, i.e., lattice distortion distribution is insensitive to $EBSP_0$ choice [40].

Existing criteria for $EBSP_0$ selection include: (1) points with low GND density or low Kernel average misorientation (KAM) [63] based on the Hough measured local grain misorientations; (2) points with high image quality (IQ), which may have a low defect density within its electron interaction volume, and is therefore assumed to be a low-strained region of a polycrystalline material [64]. However, IQ does not carry a clear physical meaning [65], and the magnitudes of the measured relative lattice distortion are insensitive to the IQ of $EBSP_0$ [40]; (3) $EBSP_0$ can also be manually selected to be far from potential stress concentrations such as grain boundaries, inclusions, or cracks [40] using subjective criteria. These criteria assume these parameters can indicate the strain conditions at the reference point, producing accurate measurements of up to 3.2×10^{-4} elastic strain [31]. However, experimental measurements point to the inaccuracy of HR-EBSD in determining the out-of-plane shear strain components distribution and magnitude [66].

Here, a thorough investigation of the effect of the $EBSP_0$ on the elastic strain, rotation and GND density maps – including magnitude and distribution – was conducted for both brittle and ductile crystal systems. This work introduces a new objective method to select an EBSP0 that maximises HR-EBSD measurement precision. The main difference is that the new method considers HR-EBSD quality metrics for all points that use the $EBSP_0$ as a reference. In contrast, existing methods consider conventional EBSD quality metrics related to the $EBSP_0$ alone.

2. Methodology

2.1. Materials and EBSD mapping

Two different materials, duplex stainless steel and silicon, were used to provide samples representing a face centre cubic ductile crystal (austenite, high plastic strain), a body center cubic ductile crystal (ferrite, low plastic strain) and a cubic single-crystal with very low dislocation density, below the noise floor of HR-EBSD lattice rotation measurements (semiconductor-grade silicon). All are model materials for EBSD analysis as the polished surface does not oxidize further, and high-quality patterns can be acquired in a reasonable time.

The 1st set of samples was taken from a large (~200 mm thickness) forging of Zeron 100 duplex stainless steel (UNS: S32760 [67]) with a

[2] Strain, distortion, and deformation can refer to several quantities in different fields. Therefore, we define our use of these terms (in italics) as follows. A mechanically loaded object changes shape in response to applied load; when measured in a mechanical test frame, it is called (total) engineering strain. Plastic strain is called the shape change that persists after the macroscopic load is removed. On the microscale, plastic deformation in most crystalline materials is accommodated by dislocation glide and deformation twinning. However, dislocations are also generated in a material as plastic deformation progresses, and dislocations with similar crystallographic character and sign that end up near each other in a material (e.g., lined up at a slip band) can be characterised as geometrically necessary dislocations (GNDs). Increasing plastic strain in a polycrystal also elastically distorts the crystal lattice to accommodate crystal defects (e.g., dislocation cores), groups of defects (e.g., dislocation cell walls), and maintains compatibility at polycrystal boundaries. This lattice distortion can be expressed as a deformation gradient tensor, which can be decomposed into elastic strain (symmetric) and lattice rotation (antisymmetric) components [99]. In this work, we use the term lattice distortion as a general term to refer to elastic distortion components derived from the deformation gradient, elastic strain, and lattice rotation tensors.

nominal composition of 25% Cr, 7% Ni, 3.6% Mo, 0.7% Cu, 0.7% W, 0.22% N that was aged at 475 °C for 100 hrs in air. This duplex stainless steel contains face-centred cubic austenite in a matrix of a body-centred cubic ferrite with a volume fraction of 58% [68]. During this heat treatment, the decomposition of the ferrite into Fe-rich nanophase (α') and Cr-rich nanophase (α'') occurs with G-phase precipitation [69–71], which increases the ferrite hardness while the hardness of the austenite phase remains unchanged [72–74]. This gives a sample with both face-centre cubic (austenite) and body-centre cubic (ferrite) phases [75].

EBSP quality is extremely sensitive to surface preparation [76]. The aged stainless steel specimen surfaces were prepared by grinding on SiC papers (240 to 4000 grit), polishing using diamond paste (from 9 to 1 μm) and then 50 nm colloidal silica (2 h, 50 r.p.m speed and 5 N force) to produce a mirror-flat surface without artefacts. The specimens were ultrasonically cleaned for 20 min using ethanol, rinsed with deionised water, and dried with a hot air blower.

The single-crystal silicon samples did not require surface preparation. Instead, they were cleaved from a pre-polished (001) single-crystal silicon wafer with a thickness of 0.5 mm. Silicon was selected as it deforms elastically with no plasticity at room temperature [77].

The samples of both materials were positioned between the jaws of a 2 kN 70° pre-tilted loading stage (Deben® MT2000E) inside a Carl Zeiss Merlin field emission gun scanning electron microscope (FEG-SEM). The SEM chamber and loading stage were plasma cleaned and purged together before the sample was deformed in displacement control by the movement of one jaw. The Si samples were compressed to grow a brittle crack, and the stainless steel samples were plastically deformed using uniaxial tension and three-point bending.

EBSD maps were collected from the *in-situ* strained sample using a 1600 × 1200 pixel Bruker eFlash CCD camera with no additional lens distortion correction. Before each observation, the setup was left to stabilise for 30 min at fixed crosshead displacement. The microscope conditions were 10 nA/20 kV beam current/voltage and 18 mm working distance for all materials. EBSPs were saved as an 800 × 600 pixel image, 16-bit depth, with 100 ms exposure time per pattern, and a step size of 75 nm for the stainless steel and 250 nm for the silicon. These conditions provided a practical time for measurement while minimising sample drift [28,59,78–80].

2.2. $EBSP_0$ effect analysis

After excluding points with a geometrical necessary dislocation (GND) density higher than the grain average (after removing the outliers), which was calculated using MTEX [29]; the reference $EBSP_0$ for each grain can be selected as a point that is remote to stress concentrations as indicated by the GND density (or KAM instead) map that has a high-quality pattern, low GND density, and an orientation close to the grain's mean orientation. $EBSP_0$ selected using this method will be termed '*Native*' in this work. Then, 50 points were randomly selected from a pool of ~15% of the highest-quality patterns to evaluate the effect of $EBSP_0$ selection on the measured HR-EBSD data. The IQ of these randomly selected patterns varied by less than 2% of their average value. Each of the 50 patterns was used in HR-EBSD calculations to map the grain's elastic strain, rotation and GND density distributions.

HR-EBSD analysis was performed using in-house MATLAB software (XEBSD) [24]. EBSP re-mapping was used to minimise strain errors due to large misorientations (>1.5°); in the second pass, the EBSPs were re-mapped to an orientation close to $EBSP_0$ by using the local rotation matrix estimated from the first pass [81]. The elastic constants (in GPa) for the ferrite (α) are: $C_{11} = 230$, $C_{44} = 117$, $C_{12} = 135$, for the austenite (γ) are: $C_{11} = 231.4$, $C_{44} = 116.4$, $C_{12} = 134.7$ [82], and for (001) silicon are $C_{11} = 165.7$, $C_{44} = 79.6$, $C_{12} = 63.9$ [83]; all were transformed to the crystal frame of reference via the Euler angles [84]. The pattern centre (PC) shift due to beam movement during acquisition was corrected using AstroEBSD [85], and 30 ROI were selected from each EBSP for cross-correlation. The ROI size is 256×256 pixels, and the

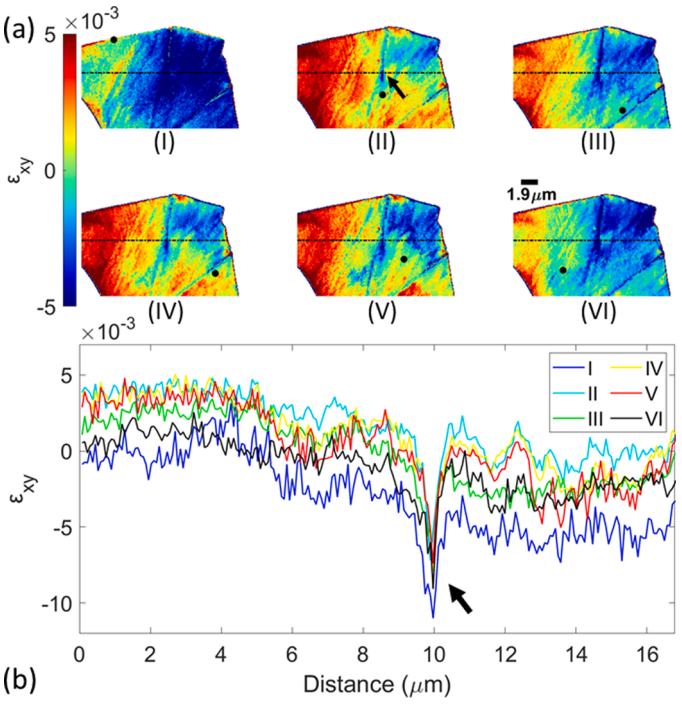

Fig. 1. (a) In-plane shear strain (ε_{xy}) fields in a ferrite grain, obtained using six different patterns as the reference $EBSP_0$. A black dot indicates the position of the reference pattern in each case. (b) The line profile of the in-plane shear strain along the dotted line. The black arrow points to the value ahead of the linear feature (i.e., deformation twin) located in the middle of the grain (see Fig. 2). V and VI are the '*Native*' and '*Chosen*' $EBSP_0$, respectively. The IQ values of points I to VI are 0.4019, 0.4419, 0.4288, 0.4563, 0.4400 and 0.4419. The sample is at 15% engineering strain, as detailed in reference [87].

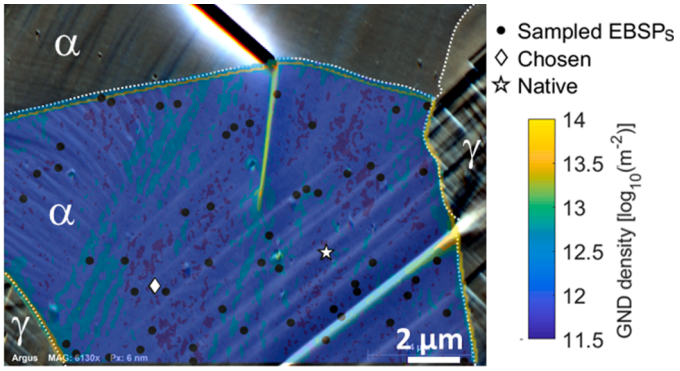

Fig. 2. Geometrical necessary dislocation (GND) density map overlaid over a forescatter electron (FSD) image for the field of view with the location of 52 EBSPs (50 random + *Native* + *Chosen*) in the example ferrite grain. One '*Native*'-ly selected (white star), 50 were randomly '*Sampled*' (black points), and another '*Chosen*' (white diamond). The average GND density is 11.85 ± 0.74 $\log_{10}(m^{-2})$.

calibrated EBSP pixel size is 18 μm. No further angular effect from drift was expected as the field of view was small (~20 × 15 μm^2), and the samples were all conductive [86]. GND density was estimated from the local lattice curvature using the method implemented by Wilkinson and Randman [28].

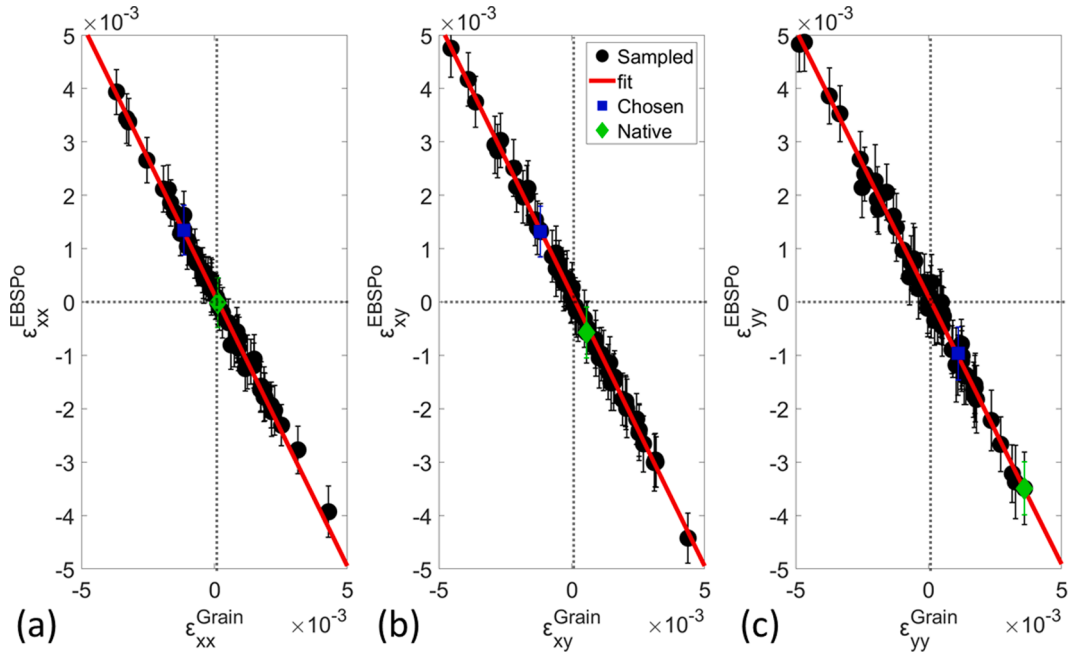

Fig. 3. Grain (field value) and $EBSP_0$ (local value) averaged (a) ε_{xx}, (b) ε_{xy}, and (c) ε_{yy} strains for the selected reference patterns with a correlation coefficient of 0.99 across the three maps. Only the standard deviation in the $EBSP_0$ local value is shown as the standard deviation for all the points in the grain is large.

3. Results

3.1. Body center cubic ferrite

The aged duplex stainless steel (DSS) sample was deformed in uniaxial tension, and then a ferrite grain was EBSD characterised to investigate the effect of the reference pattern. Fig. 1a shows the grain's elastic field (in-plane shear strain) calculated relative to six reference patterns. These six references all have a high IQ compared to other available patterns in the grain. Four points were selected randomly from

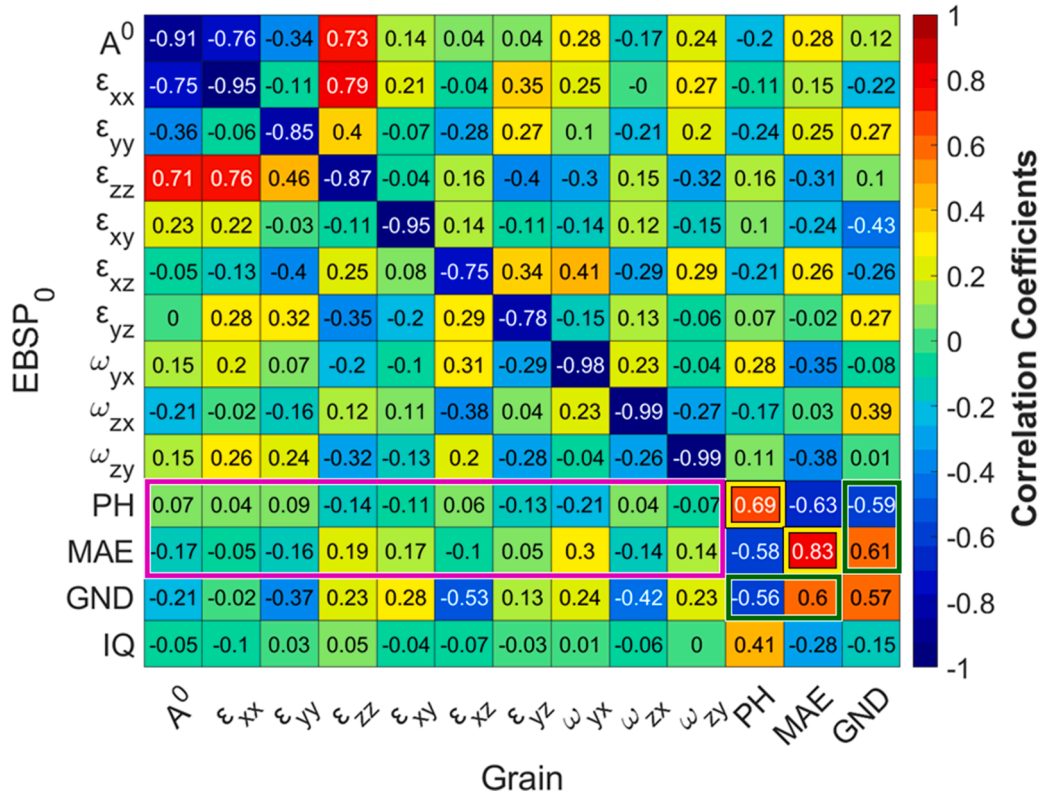

Fig. 4. Correlation coefficients between the local conditions at the $EBSP_0$ point, as averaged across the other HR-EBSD maps calculated using different EBSPs (labelled $EBSP_0$), and the conditions at the grain, as averaged from all the points within the grain (labelled 'Grain'), for the ferrite grain in aged duplex stainless steel. Negative values indicate an inverse linear relationship.

the subset of high IQ; the fifth is the '*Native*' reference point, as discussed above. The sixth is the optimal point '*Chosen*' by the iterative selection method developed in this work, and the logic behind this will be explained subsequently. The locations of the '*Native*' and '*Chosen*' points are shown in Fig. 2.

Using different $EBSP_0$ as a reference influenced the resultant in-plane shear strain distribution. The 1st selected point (Fig. 1a, point I) is near a low-angle grain boundary, where the grain misorientation is $< 0.5^{\circ}$ Despite this low angle, the region near the subgrain boundary, where the $EBSP_0$ has been selected from, is likely to have high localised strains (in this case, a positive in-plane shear strain); thus, its selection as a reference causes the relative strains measured in the grain to be shifted towards the negative direction. This is illustrated by the line profile (dark blue in Fig. 1b), which shows that the in-plane shear strain magnitude is shifted towards negative shear strains compared to the other references. The 2nd point (Fig. 1a, point II) is at the centre of the grain and leads to significantly more positive strains (light blue line profile in Fig. 1b). The 3rd point is close to a linear feature (i.e., deformation twin) in the grain (marked by the arrow in Fig. 1b), and the 4th point (Fig. 1a.III) has the highest IQ in the grain. These references give strain profiles intermediate between points I and VI, as does the 5th reference point (V), the '*Native*' reference. The 6th '*Chosen*' reference gives similar strains to point III. Generally, the difference between the lines profile is not due to an offset but noticeable non-linear changes in the distribution.

The set of 50 randomly selected high-quality reference points with a mean of 0.4384 ± 0.0090, in addition to the '*Native*' point with an IQ of 0.4400 and the '*Chosen*' point with an IQ of 0.4419, marked in Fig. 2, which also shows the GND density map superimposed on the forescatter electron image. The high GND density along the deformation twin boundaries is apparent. The points of high IQ are generally at locations with low GND density (see the supplementary information: A). These references were used individually to produce 52 HR-EBSD maps in total.

The effect of the local conditions at each $EBSP_0$ can be observed by considering the 52 HR-EBSD maps obtained from the 50 high-quality reference patterns randomly selected plus '*Native*' and '*Chosen*' EBSPs. To do this, the average strains in the HR-EBSD map arising from each $EBSP_0$ were compared with the conditions at the $EBSP_0$ in the 51 other HR-EBSD maps. These results are shown in Fig. 3. Fig. 3 shows the relationship between the grain's average strains relative to a single $EBSP_0$ (ε^{Grain}, horizontal axis), and the average strain measured at this $EBSP_0$ point when using the other 50 $EBSP_0$ (ε^{EBSP0}, vertical axis). All three strain components show an inverse linear correlation; this is expected because the strains at the grain are measured relative to the strain state at $EBSP_0$, which clearly shows the HR-EBSD map's dependency on the reference pattern choice, even from a set of high-quality references. The '*Chosen*' $EBSP_0$ is near the middle of the strain distribution for all three strain components; this most likely contributes to a high cross-correlation precision as it minimises the distortions between the $EBSP_0$ and other points in the grain to around half of the strain distribution range. In contrast, the '*Native*' $EBSP_0$ is near the middle of the strain distribution range for ε_{xx} and ε_{xy} components but at the negative end of the ε_{yy} strain distribution range, which leads to a larger maximum ε_{yy} distortion with correspondingly higher measurement uncertainties.

The correlation coefficients between the local conditions at the $EBSP_0$ point, as averaged across the other HR-EBSD maps calculated using different EBSPs (labelled $EBSP_0$), and the conditions at the grain, as averaged from all the points within the grain (labelled 'Grain'), are summarised in Fig. 4; for parameters that include: the lattice distortion components, e.g., determinant of the deformation gradient tensor (A^o), in Eq. (1) where n is the total of points, strain ε_{ij}, rotation ω_{ij}, and GND density, IQ, pH which is the (mean) cross-correlation peak height normalised by the value from the reference self-correlation in each case, and the mean angular error (MAE), which is a quantitative measure of the difference between the pattern shift at each segmented region (ROI) from the EBSP, and the best (least-square) fit solution, all obtained after re-mapping. In general, the lower the MAE, the higher the precision of the solution [81].

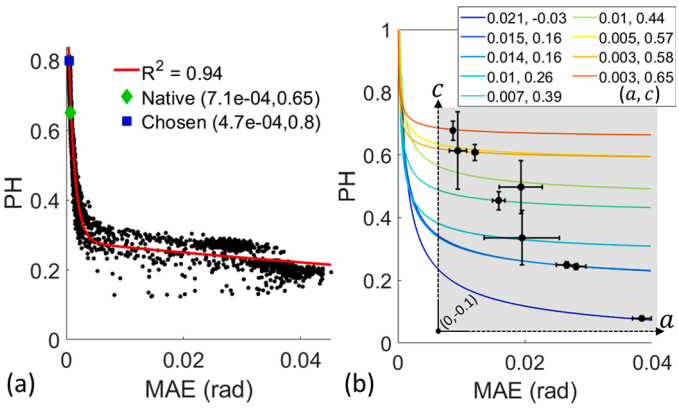

Fig. 5. (a) Cross-correlation peak height (pH) and mean angular error (MAE) for all points inside the grain averaged across all different 51 HR-EBSD maps and fitted with an inverse square root function. (b) Fitting coefficients were obtained by applying the analysis to 9 HR-EBSD maps deformed in uniaxial tension and three-point bending. The variance indicates the quality of the fitting of a and c.

$$A^o = \frac{1}{n}\sum_{el=1}^{n} |F_{ij}|_{el}, \quad i = j = x, y, z \tag{1}$$

The correlations were quantified through Pearson's correlation coefficient [88] implemented in the MATLAB® *corrcoef* function (Eq. (2)). Each dataset (A,B) was first normalised using the mean (σ) and standard deviation (μ) before finding the linear correlation coefficient (ρ) of two datasets with N number of observations.

$$\rho(A,B) = \frac{1}{N-1}\sum_{i=1}^{N}\left(\frac{\overline{A_i - \mu_A}}{\sigma_A}\right)\left(\frac{\overline{B_i - \mu_B}}{\sigma_B}\right) \tag{2}$$

The same analysis was applied to EBSD maps in 8 different grains of the body-centered cubic ferrite (386 HR-EBSD maps, at different engineering strains – see the supplementary information: A). The correlation coefficients between the $EBSP_0$ and the grain are presented in Fig. 4 by averaging the correlation coefficients from 9 sets of analyzes.

The diagonal of Fig. 4 shows a strong inverse correlation between the field and local reference pattern status in all of the strain and rotation tensor components because the grain's average lattice distortion components are measured relative to the local $EBSP_0$ values. The correlation is stronger for the rotations than for the strains because measurement noise forms a higher proportion of the measured elastic strains than for lattice rotations. Typical lattice rotations produce EBSP ROI shifts, which are an order of magnitude larger than elastic strains. This indicates that a reference pattern deformed in tension will directly reduce the tensile strain magnitudes of the resultant map while indirectly influencing the other component magnitude and the strain's distribution.

The lattice distortion components (in 'Grains' and '$EBSP_0$') are insensitive to the local cross-correlation quality metrics (i.e., pH and MAE, magenta box annotation in Fig. 4 for 'Grains' components). However, the correlation is limited to linear relationships. Significantly, pH and MAE both have positive diagonal correlation coefficients (yellow boxes in Fig. 4), which shows that $EBSP_0$ with high local pH tend to produce HR-EBSD maps with high pH, and $EBSP_0$ with low local MAE produce maps with low MAE. There is also considerable interaction between the local $EBSP_0$, grain's average GND density, and pH and MAE values (green boxes in Fig. 4). For example, high local GND density at the $EBSP_0$ reduces the grain's average pH and increases the grain's average MAE (shown in the 'pH' and 'MAE' columns of the 'GND' rows). Therefore, using $EBSP_0$ with high MAE or low pH also leads to overestimated GND densities in the grain.

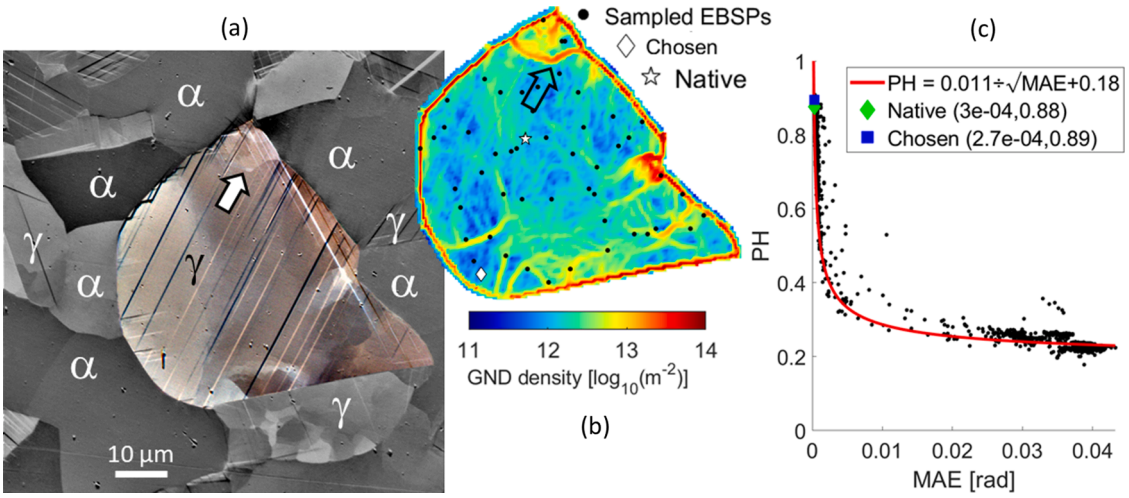

Fig. 6. (a) Forescatter electron (FSD) image with the other grains grey-scaled to accentuate the grain being examined. (b) Estimated geometrically necessary dislocations (GND) density map with the location of the 50 randomly selected $EBSP_0$ plus '*Native*' and '*Chosen*'. (c) Cross-correlation peak height (pH) and mean angular error (MAE) for all points inside the grain were averaged across all 51 HR-EBSD maps and fitted with an inverse square root function to find the '*Chosen*' pattern. The goodness of fit (R^2) equals 0.79. The sample is at 4% engineering strain; see the supplementary data: B.

All pH and MAE data points inside the grain (33 177 points) were averaged across the 51 HR-EBSD maps to infer the local response to different $EBSP_0$. These are presented in Fig. 5a, and fitted by an empirical Eq. (3), where a and c are 0.014 and 0.16, respectively. The same was done for data sets from the 9 analyzed grains (Fig. 5b), which finds an inverse relationship between c and a.

$$\mathrm{pH} = a \Big/ \sqrt{\mathrm{MAE}} + c \tag{3}$$

Figs. 4 and 5 show that using the local conditions at the $EBSP_0$ as indicated by the pH and MAE can be used as a proxy metric to estimate the map's average pH and MAE values when searching for an $EBSP_0$. From this, it can be postulated that the optimum $EBSP_0$ should offer the highest cross-correlation coefficient (high pH) with the lowest fitting errors (low MAE) since such a pattern has high quality and is close to the average grain orientation. Objectively, this is the point on the EBSD map with the highest grain's average pH value and the lowest grain's average MAE value. This was identified using an iterative algorithm that finds the point with the lowest MAE in the grain and then searches for the point with the highest pH. If these are not at the same point, the 2nd lowest MAE is located and compared, then the 2nd highest pH, until these coincide at the same point. This point, termed '*Chosen*', is indicated in Figs. 2, 3, and 5a.

The map labelled IV in Fig. 1 was produced using this '*Chosen*' $EBSP_0$. The grain's average pH and MAE are 0.76 and 6×10^{-4} rad compared to the '*Native*', which gave a pH of 0.76 and MAE of 8×10^{-4} rad. Although the difference in overall improvement is not significant in terms of cross-correlation parameters, the difference in strain magnitude and distribution can be seen clearly in Fig. 3b, V and IV, where the difference equates to ~450 MPa (e.g., at 5 μm along the line profile).

3.2. Face center cubic austenite

In this example, an austenite grain in the age-hardened duplex stainless steel deformed in uniaxial tension was analyzed (Fig. 6). The austenite phase shows significant plastic deformation, with planar slip, compared to the harder ferrite; the mean GND density is 12.44 ± 0.43 $\log_{10}(m^{-2})$, compared to 11.85 ± 0.74 $\log_{10}(m^{-2})$ in the ferrite example (Fig. 2). As for the previous ferrite example, 52 $EBSP_0$ were selected, with one being the '*Native*', 50 sampled randomly from the points with the highest IQ, and one '*Chosen*' using the algorithm to find the map point with the lowest MAE and highest pH. The locations of the points are marked on the map of GND density, which also shows significant plastic strain concentrations at some grain junctions. Due to the ductility of the austenite, larger lattice rotations occur, but the phantom strains were minimized by the re-mapping process [24]. The examples of strain maps (in-plane shear component) show the dependence of the strain magnitude and sign on the choice of reference pattern (Figs. 6 and 7, in which the arrow marks a subgrain boundary with low misorientation $< 0.5°$).

As in the analysis of the ferrite grain, the overall distribution of the in-plane shear strain is similar regardless of the reference choice, as highlighted by the strain peak at the sub-boundary (highlighted by an arrow in Figs. 6 and 7). However, the finer details of the distribution of strain and magnitude depend on the $EBSP_0$; for instance, a deformed point near the ferrite-austenite grain boundary (4th point in Fig. 7a.IV) renders the grain field as being negative even when the applied deformation was in tension, and '*Native*' (IV line) behave very different from '*Chosen*' (line VI) at 28 and 35 μm. A similar observation can be made for the 1st point (Fig. 7a.I), but the field is less negative, and a more positive in-plane shear is induced when the point is selected inside the sub-grain (3rd point). In general, the difference in distribution, as in the previous example, is not due to an offset but an observable change. The GND density is not very sensitive to the reference point (Fig. 7b); however, distribution fluctuated, especially at 32 μm.

The same correlative analysis used for the ferrite (Fig. 4) was applied to 3 different grain maps of the face centre cubic austenite (204 maps at different engineering strains – see the supplementary information: B). The correlation coefficients between the local conditions at the $EBSP_0$ and the grain are presented in Fig. 8 by averaging the correlation coefficients from 5 sets of analysis. This found weaker diagonal relationships between the in-plane shear strain (and consequently the stress) tensor (as indicated by the -0.32 correlation coefficient). The inverse correlation between the grain's and the reference pattern's strain components along the diagonal is less pronounced than in the ferrite phase. The local MAE strongly influences the resultant grain's averaged MAE, pH, and estimated GND density. Still, the influence of IQ of the reference pattern on the resultant field, similarly to the ferrite example, is lower.

Fitting Eq. (3) to the pH and MAE data for the austenite grain gave a and c of 0.011 and 0.18, respectively (Fig. 6c). The '*Chosen*' $EBSP_0$ had an average local pH of 0.89 and MAE of 2.7×10^{-4} rad compared to the '*Native*' local pH of 0.88 and MAE of 3×10^{-4}. The grain's average pH and MAE for the '*Chosen*' $EBSP_0$ were 0.85 and 13×10^{-4} rad, marginally different from the grain's average values using '*Native*', which gave a pH of 0.85 and MAE of 14×10^{-4} rad. However, as for the

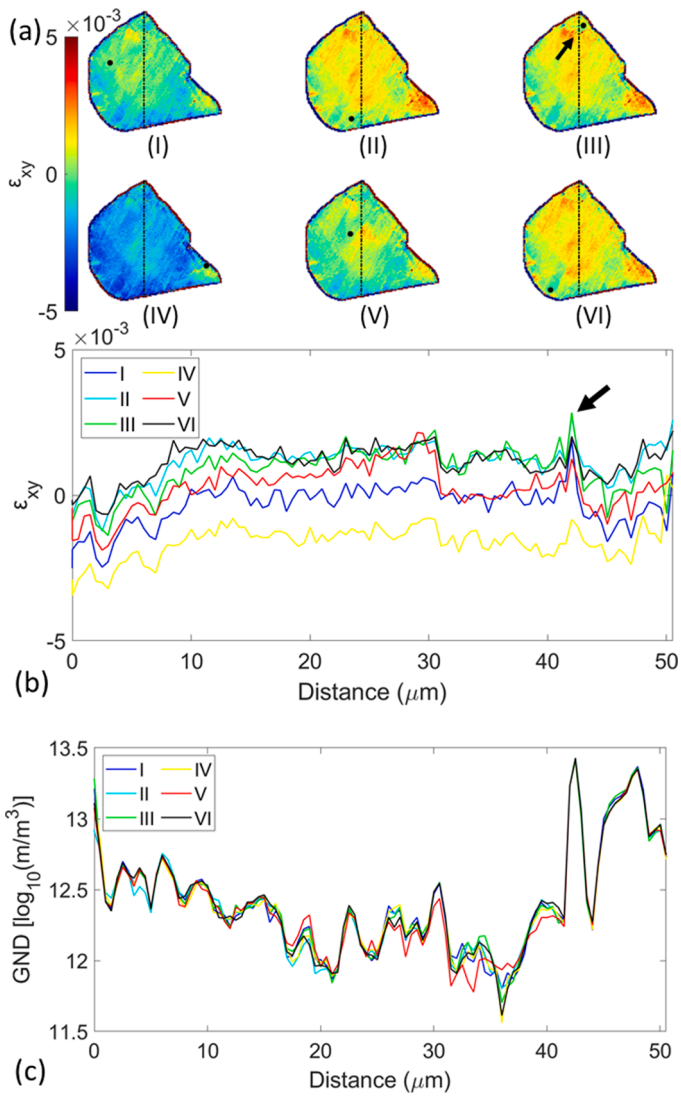

Fig. 7. (a) In-plane shear strain (ε_{xy}) fields produced using six different $EBSP_0$ in an austenite grain. A black dot indicates the position of the reference pattern. The line profile along the dotted for (b) the shear strain and (c) GND density. The arrow points to the sub-boundary, also seen in Fig. 6. V and VI are '*Native*' and '*Chosen*' $EBSP_0$. The IQ values of points I to VI are 0.4225, 0.4619, 0.4569, 0.4956, 0.4737 and 0.4794.

ferrite example, although the mean improvement in correlation parameters was not substantial, the effect on the stress magnitudes and distribution cannot be ignored, which is observed in Fig. 7, comparing V and VI, where the difference in the in-plane shear strain equates to ~250 MPa.

3.3. Silicon

EBSD maps were collected for the silicon sample around the tip of a cleavage crack as it was propagated in a quasi-static manner in 12 intervals [89]. The change between the stress maps due to different $EBSP_0$ was minimal in magnitude and distribution once the $EBSP_0$ was selected to be remote (> 12 μm) from the crack (Fig. 9a). Applying the same correlative analysis to the 12 observations (12 datasets x 52 sampled $EBSP_0$ = 624 maps) gives Fig. 10. The diagonal correlation for the lattice distortion components is similar to that observed in the ferrite, with an inverse correlation between the grain and $EBSP_0$ local average value in each tensor of the strain and rotation components. This strong correlation is also seen in MAE, but EBPS0 image quality, pH, MAE, or the choice of $EBSP_0$ do not influence the estimated GND density, because, at room temperature, silicon has no significant plasticity [90] and the dislocation density is lower than the HR-EBSD GND density measurement noise floor [28].

The '*Chosen*' $EBSP_0$ was taken as the point with the highest pH and lowest MAE, and a trend was observed between the fitting parameters for the 12 datasets as in the previous analysis of the ferrite (Fig. 10). Using the '*Chosen*' compared to '*Native*' did not significantly reduce the elastic strain but slightly improved pH and MAE in the calculated field (see the supplementary information: C).

4. Discussion

4.1. The effect of $EBSP_0$

The correlation coefficients are summarised in Fig. 11 for the elastic silicon (Si) sample and the ferrite (Fe-α) and the austenite (Fe-γ) phases, which deformed plastically to different degrees. The figure shows correlation coefficients between the local conditions at the $EBSP_0$ point and the averaged conditions at the grain for different parameters: the average elastic deformation gradient tensor (A^0) determinant, maximum in-plane principal strain (ε_{Max}), rotation magnitude ($\omega_T = \sqrt{\omega_{32}^2 + \omega_{13}^2 + \omega_{21}^2}$), peak height (pH), mean angular error (MAE) and GND density, and materials: the ferrite (Fe-α) and austenite (Fe-γ) phase of age-hardened DSS, and Silicon (Si). Fig. 11 shows that correlations between the local conditions at the $EBSP_0$ point and the averaged conditions at the grain are material-dependent and impact the calculated field parameters.

The full-field elastic deformation gradient and the strain strongly depend on the absolute lattice distortion at the $EBSP_0$, which is expected for a relative strain measurement. However, this correlation weakens with increasing plastic deformation in the grain, which shows that the $EBSP_0$ selection is still important even if only relative strains are considered, especially if the material is plastically deformed. However, the rotation magnitude (ω_T) and MAE have a high positive correlation coefficient unaffected by the material plasticity. This confirms that minimizing the local $EBSP_0$'s MAE is always a good way to minimize the grain's MAE in both plastically and elastically deformed materials.

In the plastically deformed grains, the grain's average GND density is positively correlated with local $EBSP_0$ GND density, even though GND density is nominally considered insensitive to $EBSP_0$ selection. Within the set of randomly selected reference points with high IQ, the $EBSP_0$ seems to affect the GND density distribution and magnitude, which contradicts the assumption that HR-EBSD can precisely determine the lattice distortion gradient independently of the $EBSP_0$ [40,61,62]. $EBSP_0$ selection can also cause individual features in the GND density map to appear or disappear (compare line profiles of Fig. 7c). However, the GND density is typically reported in log scale maps (Fig. 7c); thus, this influence (roughly less than ± 0.04 $\log_{10}$ (m/m^{-3})) is relatively small.

The degree of correlation between local-$EBSP_0$'s MAE and pH with the grain's average GND density is material-dependent. For example, the ferrite showed a strong correlation between the resultant map's pH and MAE with the $EBSP_0$ image quality (IQ) and GND density, where an $EBSP_0$ with high IQ and low GND density produced a map with high pH and low MAE. This is consistent with the widespread use of the '*Native*' selection (which selects $EBSP_0$ with high IQ and low GND density) across the literature [30,62,91–95], as this is likely to produce EBSD maps with relatively high pH and low MAE. However, this correlation is weaker for the austenite grain and is negligible for the Si crystal.

Thus, the lattice distortion arising from residual elastic strains and crystal defects within the electron interaction volume at the reference point affects the pH and MAE, as crystal defects such as dislocations reduce pH and increase MAE. In contrast, residual elastic strain mainly increases MAE by changing the position of zone axes within the diffraction pattern. This further shows the significance of local lattice

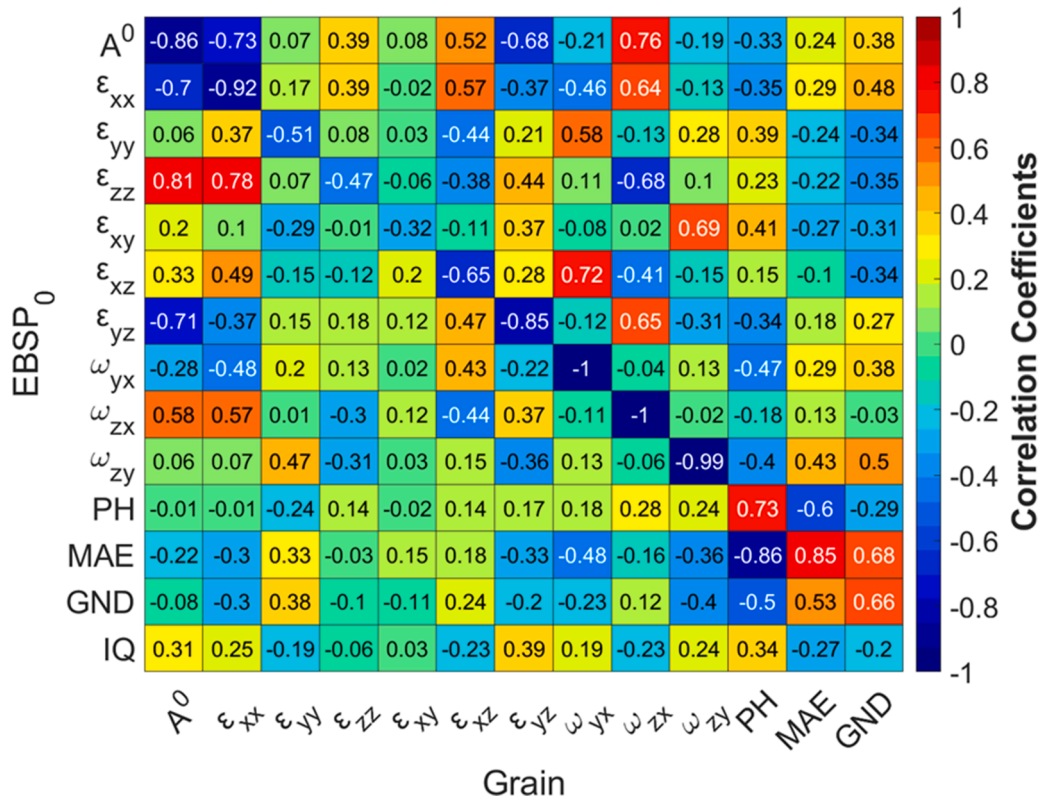

Fig. 8. Correlation coefficients between the local conditions at the $EBSP_0$ point, as averaged across the other HR-EBSD maps calculated using different EBSPs (labelled $EBSP_0$), and the conditions at the grain, as averaged from all the points within the grain (labelled 'Grain'), for the austenite grain in aged duplex stainless steel. Negative values indicate an inverse linear relationship.

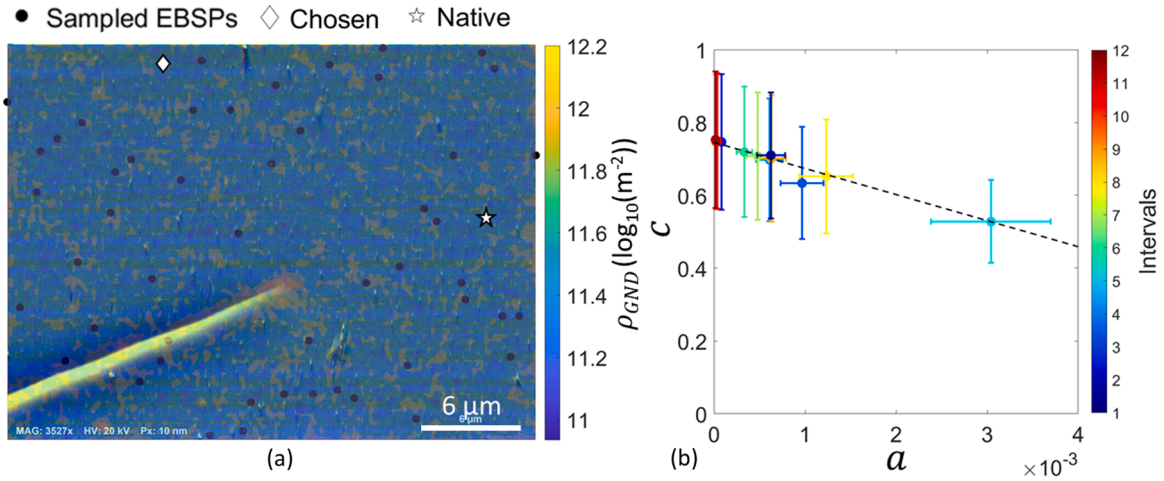

Fig. 9. (a) Forescatter electron (FSD) image for the crack number propagating in (001) silicon-crystal deformed in compression overlayed with the estimated GND density map that includes the location of the 52 $EBSP_0$, including '*Native*' and '*Chosen*'. (b) Fitting coefficients *a* and *c* from Eq. (4) with the legend indicating the experiment intervals.

rotation-induced perturbations on patterns, which increase with GND density. Note that the correlation coefficient discussed here (i.e., Pearson correlation coefficient) is a linear correlation coefficient that ignores non-linear components of a correlation relationship that may exist.

The choice of $EBSP_0$ changes the spatial distribution of both lattice distortion and GND density maps. This is contrary to the adopted assumption that all relative lattice distortion values are only shifted from the absolute distortions by a constant equal to the absolute distortion at $EBSP_0$ (which could be identified, for example, using a CPFE simulation [56,57]. Recently, an exciting approach to studying this phenomenon was made by simulating an EBSP from a deformed volume of interaction [18,96]. The reverse engineering of the problem by applying a lattice distortion to the EBSP helps separate what each deformation component does to the EBSP geometry, the deformation's effect on intensity distributions in the EBSP, pattern distortion from instruments, and can provide insights into how the correlation between sharp and blurred patterns can be used to estimate plastic strains.

Furthermore, there is no apparent connection between $EBSP_0$'s IQ and $EBSP_0$'s local lattice distortion. This is contrary to qualitative studies that used pattern characteristics as indicators of elastic strain

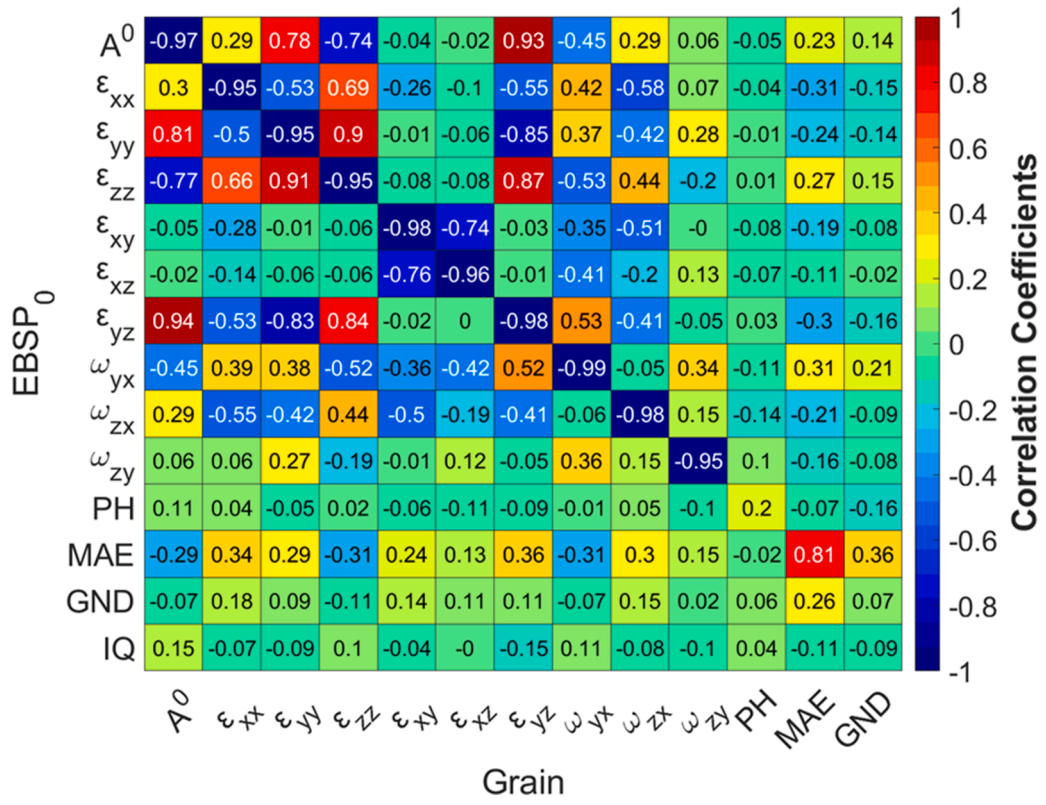

Fig. 10. Correlation coefficients for the grain average (Grain) and reference point average ($EBSP_0$) averaged for 12 Si maps. The minus sign indicates an inverse relationship.

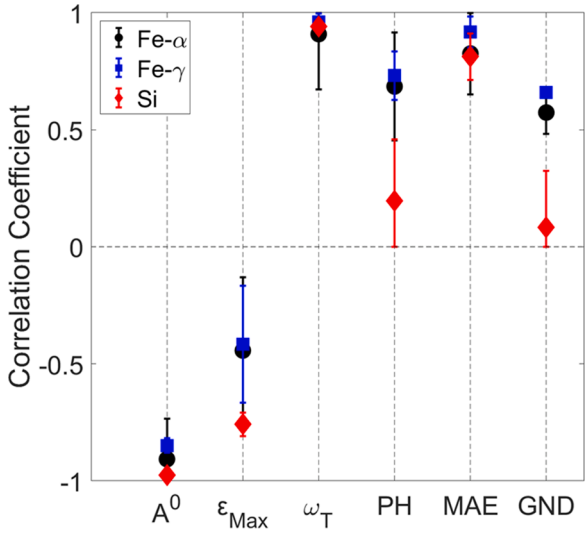

Fig. 11. Linear correlation coefficients between the local conditions at the $EBSP_0$ point and the averaged conditions at the grain for the ferrite (Fe-α) and austenite (Fe-γ) phase of age-hardened DSS, and Silicon (Si). The analysis considers the average deformation gradient tensor determinant (A^0), maximum in-plane principal strain (ε_{Max}), rotation magnitude ($\omega_T = \sqrt{\omega_{32}^2 + \omega_{13}^2 + \omega_{21}^2}$), correlation peak height (PH), mean angular error (MAE) and GND density.

gradient [97]; however, we only considered high-quality patterns, and Wright et al. [98] asserted that due to the relationship between electron beam spot size and probed pattern degradation, qualitative analysis that uses IQ is only adequate for a tungsten filament scanning electron microscope and not a FEG (field emission gun) microscope, which was used here.

When the pH and MAE of the grain were averaged across the 51 HR-EBSD maps, the result could be fitted to an empirical equation (Eq. (3)) where the pH is related to the inverse of the square root of MAE through two coefficients, *a* and *c*. This inverse relationship between the pH and MAE encapsulates the effect of the stored dislocations on the blurring of the patterns and the impact of lattice distortion on the shifts in the zone axes. The optimum $EBSP_0$, i.e., the '*Chosen*' reference points, should offer the lowest errors (low MAE) with the highest cross-correlation (high pH). Such a pattern naturally has high quality and is close to the average grain orientation. High pH indicates low crystal defect density within the interaction volume, which blurs the EBSD pattern due to local lattice distortions near defect centres such as dislocation cores. In the case of GNDs, a lattice rotation gradient is also produced across the interaction volume [3]. Low MAE relates to the consistent description of the strain state, i.e., it reduces the uncertainty that arises from the unknown absolute lattice distortion at the $EBSP_0$ on the calculated lattice distortion field by improving the HR-EBSD measurement precision (less random point-to-point noise). Thus, the search algorithm applied to select the optimum $EBSP_0$ gives more weight to MAE as the induced noise (from pattern acquisition or stored crystal defects) is directly affected by the local MAE. pH is also more affected by MAE as plasticity increases, with the correlation between local MAE and grain pH increasing from -0.13 to -0.58, and to as high as -0.86 for the Si, Fe-α, and Fe-γ, respectively. The need for re-mapping increases due to significant lattice rotation; thus, the suitability of the $EBSP_0$ becomes more critical while reducing phantom strains [38,39].

Finally, the offset-corrected standard deviation between the six ε_{xy} line profiles in Fig. 1, without considering the measurement's mean angular error (MAE) which is a cross-correlation parameter that quantifies the imprecision in fitting the HR-EBSD pattern's shifts to a deformation gradient tensor, is $\pm 7.3 \times 10^{-4}$ (Supplementary Fig. 2). Since it is within the same magnitude of the typical HR-EBSD measurement mean (angular) error (MAE), this might imply that the spatial distribution's

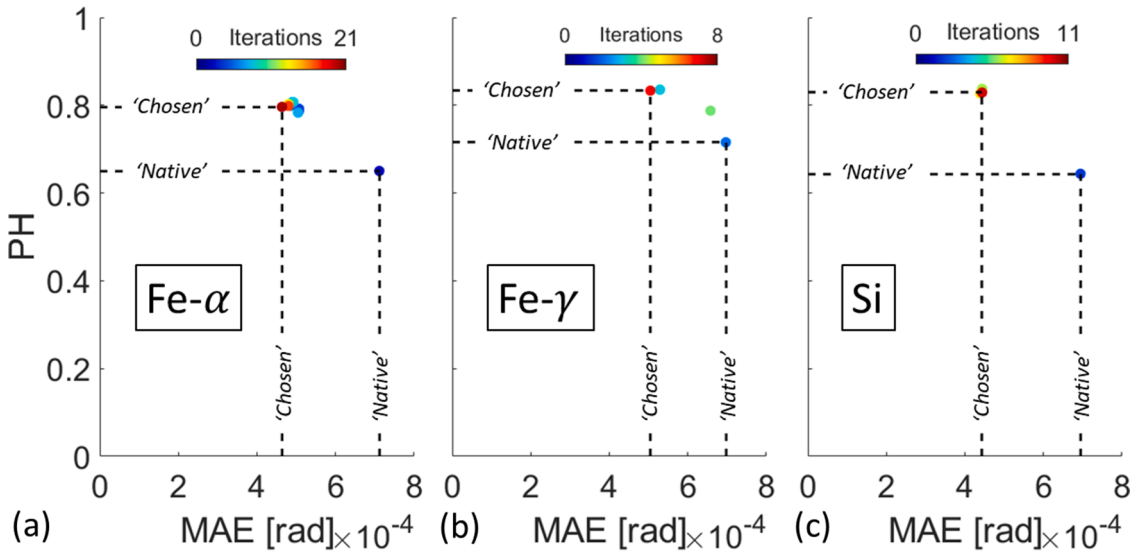

Fig. 12. Number of iterations required to find the '*Chosen*' $EBSP_0$ starting from a '*Native*' $EBSP_0$ for (a) ferrite, (b) austenite, and (c) silicon.

offset-corrected variance can be described using the MAE to quantify the noise induced due to $EBSP_0$ selection. But to make this assumption, we will need to (1) calculate the spatial distribution's offset-corrected standard deviation between HR-EBSD maps created using different $EBSP_0$ and an accurate (absolute) strain map, (2) calculate the MAE of each HR-EBSD map created using different $EBSP_0$. The correlation between (1) and (2) – for a statistically significant number of maps – will indicate whether the HR-EBSD's MAE can sufficiently describe the spatial distributions' variance; thus, the precision. However, verifying whether the MAE of different $EBSP_0$-based maps is a true measure of HR-EBSD precision, compared to a true measurement, has never been done, and can bring much-needed clarity about HR-EBSD (true) precision.

4.2. Selecting an $EBSP_0$

We defined the optimal reference pattern as the one that enables the most precise measurement of the deformation gradient tensor, i.e., produces the lowest average MAE in the grain [81]. Although the data being analyzed was measured *in situ* at different elastic and plastic straining levels, the method explored here is indifferent to whether the material is relaxed or loaded. Therefore, the method presented in this work is to select a reference pattern to maximise the precision of the elastic strain measurements, not the accuracy, which depends on the absolute strain state of the reference pattern, and that is generally unknown.

This approach operates under the substantiated hypothesis[3] that a good $EBSP_0$, which produces an HR-EBSD map with low grain's average MAE and high grain's average pH values, tends to show up as a point with low local MAE and high local pH in the HR-EBSD map computed with respect to a different $EBSP_0$. The $EBSP_0$ selected using the MAE and pH-based criteria were termed '*Chosen*' in this work. In practice, the $EBSP_0$ search algorithm uses both the MAE and pH in the optimisation process; the strong inverse correlation between these two parameters (as shown in Figs. 5 and 6) means there is no harm in using them both, and this could improve the robustness of the selection process by excluding rogue patterns with poor cross-correlation quality, but erroneously precise solutions (e.g., measuring cross-correlation shifts of all zeros).

[3] In other words, there is a strong correlation between the grain's average MAE and PH (of a selected $EBSP_0$), and its local MAE and PH (computed using any other $EBSP_0$). The strength of these correlations is shown for three different crystal types in the Results section, in Figs. 4, 8, and 10.

The optimal $EBSP_0$ offers (1) maximum EBSD cross-correlation quality; and (2) the most precise fit to the deformation gradient tensors from the measured ROI shifts across the entire grain, i.e., all EBSPs which use it as a reference point. Expressed as HR-EBSD quality metrics, this is the $EBSP_0$ with (1) the highest grain's average pH; and (2) the lowest grain's average MAE. Using these selection criteria, a brute-force search for the optimal $EBSP_0$ would require the computation of as many HR-EBSD maps as there are points in the grain, which would be computationally unfeasible. Even interrogating 51 random $EBSP_0$, as we did in this paper, is very computationally expensive.

A more viable approach uses an iterative algorithm starting with the '*Native*' $EBSP_0$. The $EBSP_0$ for each iteration is selected from the local MAE and pH values averaged over all previous map iterations until the grain's average MAE and pH values converge at a low minimum value. This approach is more computationally efficient. As shown in Fig. 12, the optimality of the $EBSP_0$ is substantially increased just one iteration after the initial '*Native*' $EBSP_0$, with a suitable $EBSP_0$ being found after only three iterations with a resultant map that is comparable to one produced from an $EBSP_0$ found after 51 iterations, i.e., '*Chosen*' $EBSP_0$.

5. Conclusion

The effect of the reference pattern ($EBSP_0$) on HR-EBSD analysis of deformation in cubic crystals with different degrees of plastic deformation has been studied to conclude that the local lattice distortion at the $EBSP_0$ influences the resultant HR-EBSD map, e.g., a reference pattern deformed in tension will directly reduce the HR-EBSD map tensile strain magnitude while indirectly influencing the other component magnitude and the strain's spatial distribution. Furthermore, the choice of $EBSP_0$ slightly affects the GND density distribution and magnitude, and choosing a reference pattern with a higher GND density reduces the cross-correlation quality, changes the spatial distribution and induces more errors than choosing a reference pattern with high lattice distortion. Additionally, there is no apparent connection between $EBSP_0$'s IQ and $EBSP_0$'s local lattice distortion.

The study revealed an empirical relationship between the cross-correlation peak height (pH) and the mean angular error (MAE), in the form of $\mathrm{pH} = a/\sqrt{\mathrm{MAE}} + c$, where a and c are fitting parameters. This relationship was used – iteratively – to find the optimal $EBSP_0$, which improved the HR-EBSD precision. Although our method does not enable absolute strain measurement in HR-EBSD; it does increase the precision of lattice distortion maps and might complement methods based on enhancing the probed field by independently approximating the strain at

the $EBSP_0$ point.

CRediT authorship contribution statement

Abdalrhaman Koko: Conceptualization, Methodology, Software, Investigation, Formal analysis, Writing – original draft, Visualization. **Vivian Tong:** Writing – review & editing. **Angus J. Wilkinson:** Software, Writing – review & editing, Supervision. **T. James Marrow:** Resources, Writing – review & editing, Supervision, Funding acquisition.

Declaration of Competing Interest

The authors declare that they have no known competing financial interests or personal relationships that could have appeared to influence the work reported in this paper.

Data availability

Data will be made available on request.

Acknowledgments

We thank Dr Roger Francis (Rolled Alloys www.rolledalloys.com) and Professor Peter Wilshaw (University of Oxford) for supplying the specimen materials. The authors acknowledge the use of characterisation facilities within the David Cockayne Centre for Electron Microscopy (DCCEM), Department of Materials, University of Oxford, alongside financial support provided by the Henry Royce Institute (Grant ref EP/R010145/1). Abdalrhaman Koko is supported by an EPSRC research studentship (Grant ref EP/N509711/1).

References

[1] A. BL, S.I. Wright, K. Kunze, Orientation imaging: the emergence of a new microscopy, Metall. Trans. A 24 (1993) 819–831, https://doi.org/10.1007/BF02656503.
[2] F.J. Humphreys, Review Grain and subgrain characterisation by electron backscatter diffraction, J. Mater. Sci. 36 (2001) 3833–3854, https://doi.org/10.1023/A:1017973432592.
[3] A.J. Wilkinson, P.B. Hirsch, Electron diffraction based techniques in scanning electron microscopy of bulk materials, Micron 28 (1997) 279–308, https://doi.org/10.1016/S0968-4328(97)00032-2.
[4] V. Randle, Electron backscatter diffraction: strategies for reliable data acquisition and processing, Mater. Charact. 60 (2009) 913–922, https://doi.org/10.1016/j.matchar.2009.05.011.
[5] J.I. Goldstein, D.E. Newbury, J.R. Michael, N.W.M. Ritchie, J.H.J. Scott, D.C. Joy, Backscattered electrons. Scanning Electron Microscopy and X-Ray Microanalysis, 4th ed., Springer, New York, NY, 2018, pp. 15–28, https://doi.org/10.1007/978-1-4939-6676-9_2.
[6] A. Winkelmann, G. Nolze, Analysis of Kikuchi band contrast reversal in electron backscatter diffraction patterns of silicon, Ultramicroscopy 110 (2010) 190–194, https://doi.org/10.1016/J.ULTRAMIC.2009.11.008.
[7] R.A. Schwarzer, D.P. Field, B.L. Adams, M. Kumar, A.J. Schwartz, Present state of electron backscatter diffraction and prospective developments, Schwartz AJ, Kumar M, Adams BL, Field DP, in: Electron Backscatter Diffraction in Materials Science, 53, Springer US, Boston, MA, 2009, pp. 1–20, https://doi.org/10.1007/978-0-387-88136-2_1.
[8] J.A. Venables, C.J. Harland, Electron back-scattering patterns—a new technique for obtaining crystallographic information in the scanning electron microscope, Philos. Mag. 27 (1973) 1193–1200, https://doi.org/10.1080/14786437308225827.
[9] D. Chen, J.C. Kuo, W.T. Wu, Effect of microscopic parameters on EBSD spatial resolution, Ultramicroscopy 111 (2011) 1488–1494, https://doi.org/10.1016/j.ultramic.2011.06.007.
[10] D.P. Field, Improving the spatial resolution of EBSD, Microsc. Microanal. 11 (2005) 52–53, https://doi.org/10.1017/S1431927605506445.
[11] A. Deal, X. Tao, A. Eades, EBSD geometry in the SEM: simulation and representation, Surf. Interface Anal. 37 (2005) 1017–1020, https://doi.org/10.1002/sia.2115.
[12] D.J. Dingley, V. Randle, Microtexture determination by electron back-scatter diffraction, J. Mater. Sci. 27 (1992) 4545–4566, https://doi.org/10.1007/BF01165988.
[13] B.L. Adams, Orientation imaging microscopy: emerging and future applications, Ultramicroscopy 67 (1997) 11–17, https://doi.org/10.1016/S0304-3991(96)00103-9.
[14] A. Winkelmann, C. Trager-Cowan, F. Sweeney, A.P. Day, P. Parbrook, Many-beam dynamical simulation of electron backscatter diffraction patterns, Ultramicroscopy 107 (2007) 414–421, https://doi.org/10.1016/j.ultramic.2006.10.006.
[15] N.C.K. Lassen, D.J. Jensen, K. Conradsen, Automatic recognition of deformed and recrystallized regions in partly recrystallized samples using electron back scattering patterns, Mater. Sci. Forum 157–162 (1994) 149–158, https://doi.org/10.4028/WWW.SCIENTIFIC.NET/MSF.157-162.149.
[16] P.V.C. Hough Method and means for recognizing complex patterns, 1962.
[17] A.J. Wilkinson, Methods for determining elastic strains from electron backscatter diffraction and electron channelling patterns, Mater. Sci. Technol. 13 (1997) 79–84, https://doi.org/10.1179/mst.1997.13.1.79.
[18] C. Zhu, M. de Graef, EBSD pattern simulations for an interaction volume containing lattice defects, Ultramicroscopy 218 (2020), 113088, https://doi.org/10.1016/J.ULTRAMIC.2020.113088.
[19] K.Z. Troost, P. van der Sluis, D.J. Gravesteijn, Microscale elastic-strain determination by backscatter Kikuchi diffraction in the scanning electron microscope, Appl. Phys. Lett. 62 (1993) 1110–1112, https://doi.org/10.1063/1.108758.
[20] A.J. Wilkinson, D.J. Dingley, Quantitative deformation studies using electron back scatter patterns, Acta Metall. Mater. 39 (1991) 3047–3055, https://doi.org/10.1016/0956-7151(91)90037-2.
[21] A.J. Wilkinson, Measurement of elastic strains and small lattice rotations using electron back scatter diffraction, Ultramicroscopy 62 (1996) 237–247, https://doi.org/10.1016/0304-3991(95)00152-2.
[22] A.J. Wilkinson, G. Meaden, D.J. Dingley, High resolution mapping of strains and rotations using electron backscatter diffraction, Mater. Sci. Technol. 22 (2006) 1271–1278, https://doi.org/10.1179/174328406X130966.
[23] A.J. Wilkinson, G. Meaden, D.J. Dingley, High-resolution elastic strain measurement from electron backscatter diffraction patterns: new levels of sensitivity, Ultramicroscopy 106 (2006) 307–313, https://doi.org/10.1016/j.ultramic.2005.10.001.
[24] T.B. Britton, A.J. Wilkinson, High resolution electron backscatter diffraction measurements of elastic strain variations in the presence of larger lattice rotations, Ultramicroscopy 114 (2012) 82–95, https://doi.org/10.1016/J.ULTRAMIC.2012.01.004.
[25] C. Maurice, R. Fortunier, A 3D Hough transform for indexing EBSD and Kossel patterns, J. Microsc. 230 (2008) 520–529, https://doi.org/10.1111/j.1365-2818.2008.02045.x.
[26] T.B. Britton A highest resolution electron backscatter diffraction study of titanium and its alloys. 2010.
[27] T.J. Hardin, T.J. Ruggles, D.P. Koch, S.R. Niezgoda, D.T. Fullwood, E.R. Homer, Analysis of traction-free assumption in high-resolution EBSD measurements, J. Microsc. 260 (2015) 73–85, https://doi.org/10.1111/jmi.12268.
[28] A.J. Wilkinson, D. Randman, Determination of elastic strain fields and geometrically necessary dislocation distributions near nanoindents using electron back scatter diffraction, Philos. Mag. 90 (2010) 1159–1177, https://doi.org/10.1080/14786430903304145.
[29] W. Pantleon, Resolving the geometrically necessary dislocation content by conventional electron backscattering diffraction, Scr. Mater. 58 (2008) 994–997, https://doi.org/10.1016/J.SCRIPTAMAT.2008.01.050.
[30] S. Villert, C. Maurice, C. Wyon, R. Fortunier, Accuracy assessment of elastic strain measurement by EBSD, J. Microsc. 233 (2009) 290–301, https://doi.org/10.1111/j.1365-2818.2009.03120.x.
[31] E. Plancher, J. Petit, C. Maurice, V. Favier, L. Saintoyant, D. Loisnard, et al., On the accuracy of elastic strain field measurements by laue microdiffraction and high-resolution EBSD: a cross-validation experiment, Exp. Mech. 56 (2016) 483–492, https://doi.org/10.1007/S11340-015-0114-1/FIGURES/8.
[32] T. Riedl, H. Wendrock, Reliability of high-resolution electron backscatter diffraction determination of strain and rotation variations using phase-only and cross correlation, Cryst. Res. Technol. 49 (2014) 195–203, https://doi.org/10.1002/CRAT.201300217.
[33] C. Maurice, J.H. Driver, R. Fortunier, On solving the orientation gradient dependency of high angular resolution EBSD, Ultramicroscopy 113 (2012) 171–181, https://doi.org/10.1016/J.ULTRAMIC.2011.10.013.
[34] T.J. Ruggles, G.F. Bomarito, R.L. Qiu, J.D. Hochhalter, New levels of high angular resolution EBSD performance via inverse compositional Gauss–Newton based digital image correlation, Ultramicroscopy 195 (2018) 85–92, https://doi.org/10.1016/j.ultramic.2018.08.020.
[35] T. Vermeij, J.P.M. Hoefnagels, A consistent full-field integrated DIC framework for HR-EBSD, Ultramicroscopy 191 (2018) 44–50, https://doi.org/10.1016/J.ULTRAMIC.2018.05.001.
[36] C. Ernould, B. Beausir, J.J. Fundenberger, V. Taupin, E. Bouzy, Integrated correction of optical distortions for global HR-EBSD techniques, Ultramicroscopy 221 (2021), 113158, https://doi.org/10.1016/J.ULTRAMIC.2020.113158.
[37] Q. Shi, D. Loisnard, C. Dan, F. Zhang, H. Zhong, H. Li, et al., Calibration of crystal orientation and pattern center of EBSD using integrated digital image correlation, Mater. Charact. 178 (2021), 111206, https://doi.org/10.1016/J.MATCHAR.2021.111206.
[38] by C. Maurice, R. Fortunier, J. Driver, A. Day, K. Mingard, G. Meaden, J. Kacher, C. Landon, B.L. Adams, D. Fullwood, Comments on the paper "Bragg's law diffraction simulations for electron backscatter diffraction analysis, Ultramicroscopy 110 (2010) 758–759, https://doi.org/10.1016/J.ULTRAMIC.2010.02.003.
[39] T.B. Britton, Comment on "an experimental study on evolution of grain-scale stress/strain and geometrical necessary dislocations in advanced TA15 titanium

alloy during uniaxial tension deformation, Adv. Eng. Mater. 19 (2017), 1700051, https://doi.org/10.1002/ADEM.201700051.
[40] Y. Mikami, K. Oda, M. Kamaya, M. Mochizuki, Effect of reference point selection on microscopic stress measurement using EBSD, Mater. Sci. Eng. A 647 (2015) 256–264, https://doi.org/10.1016/j.msea.2015.09.004.
[41] A.J. Wilkinson, B.T. Ben, Strains, planes, and EBSD in materials science, Mater. Today 15 (2012) 366–376, https://doi.org/10.1016/S1369-7021(12)70163-3.
[42] A. Koko, P. Earp, T. Wigger, J. Tong, T.J. Marrow, J-integral analysis: an EDXD and DIC comparative study for a fatigue crack, Int. J. Fatigue 134 (2020), 105474, https://doi.org/10.1016/j.ijfatigue.2020.105474.
[43] J. Kacher, C. Landon, B.L. Adams, D. Fullwood, Bragg's Law diffraction simulations for electron backscatter diffraction analysis, Ultramicroscopy 109 (2009) 1148–1156, https://doi.org/10.1016/J.ULTRAMIC.2009.04.007.
[44] A.W. Werner, GN and MV and FS-P and WSM. Physics-based simulation models for EBSD: advances and challenges, IOP Conf. Ser. Mater. Sci. Eng. 109 (2016) 12018.
[45] J. Alkorta, M. Marteleur, P.J. Jacques, Improved simulation based HR-EBSD procedure using image gradient based DIC techniques, Ultramicroscopy 182 (2017) 17–27, https://doi.org/10.1016/J.ULTRAMIC.2017.06.015.
[46] A. Winkelmann, G. Nolze, G. Cios, T. Tokarski, P. Bała, B. Hourahine, et al., Kikuchi pattern simulations of backscattered and transmitted electrons, J. Microsc. 284 (2021) 157–184, https://doi.org/10.1111/JMI.13051.
[47] A. Winkelmann, G. Nolze, M. Vos, F. Salvat-Pujol, W.S.M. Werner, Physics-based simulation models for EBSD: advances and challenges, IOP Conf. Ser. Mater. Sci. Eng. 109 (2016), 012018, https://doi.org/10.1088/1757-899X/109/1/012018.
[48] A. Winkelmann, Principles of depth-resolved Kikuchi pattern simulation for electron backscatter diffraction, J. Microsc. 239 (2010) 32–45, https://doi.org/10.1111/J.1365-2818.2009.03353.X.
[49] T. Vermeij, M. de Graef, J. Hoefnagels, Demonstrating the potential of accurate absolute cross-grain stress and orientation correlation using electron backscatter diffraction, Scr. Mater. 162 (2019) 266–271, https://doi.org/10.1016/J.SCRIPTAMAT.2018.11.030.
[50] T. Tanaka, A.J. Wilkinson, Pattern matching analysis of electron backscatter diffraction patterns for pattern centre, crystal orientation and absolute elastic strain determination – accuracy and precision assessment, Ultramicroscopy 202 (2019) 87–99, https://doi.org/10.1016/J.ULTRAMIC.2019.04.006.
[51] J. Kacher, J. Basinger, B.L. Adams, D.T. Fullwood, Reply to comment by maurice et al. in response to "Bragg's law diffraction simulations for electron backscatter diffraction analysis, Ultramicroscopy 110 (2010) 760–762, https://doi.org/10.1016/j.ultramic.2010.02.004.
[52] D. Fullwood, M. Vaudin, C. Daniels, T. Ruggles, S.I. Wright, Validation of kinematically simulated pattern HR-EBSD for measuring absolute strains and lattice tetragonality, Mater. Charact. 107 (2015) 270–277, https://doi.org/10.1016/J.MATCHAR.2015.07.017.
[53] T.B. Britton, C. Maurice, R. Fortunier, J.H. Driver, A.P. Day, G. Meaden, et al., Factors affecting the accuracy of high resolution electron backscatter diffraction when using simulated patterns, Ultramicroscopy 110 (2010) 1443–1453, https://doi.org/10.1016/j.ultramic.2010.08.001.
[54] J. Alkorta, Limits of simulation based high resolution EBSD, Ultramicroscopy 131 (2013) 33–38, https://doi.org/10.1016/J.ULTRAMIC.2013.03.020.
[55] B.E. Jackson, J.J. Christensen, S. Singh, M. de Graef, D.T. Fullwood, E.R. Homer, et al., Performance of dynamically simulated reference patterns for cross-correlation electron backscatter diffraction, Microsc. Microanal. 22 (2016) 789–802, https://doi.org/10.1017/S143192761601148X.
[56] T. Zhang, D.M. Collins, F.P.E. Dunne, B.A. Shollock, Crystal plasticity and high-resolution electron backscatter diffraction analysis of full-field polycrystal Ni superalloy strains and rotations under thermal loading, Acta Mater. 80 (2014) 25–38, https://doi.org/10.1016/j.actamat.2014.07.036.
[57] Y. Guo, C. Zong, T.B. Britton, Development of local plasticity around voids during tensile deformation, Mater. Sci. Eng. A 814 (2021), 141227, https://doi.org/10.1016/J.MSEA.2021.141227.
[58] A. Koko, J. Marrow, E. Elmukashfi A computational method for the determination of the elastic displacement field using measured elastic deformation field. To Appear 2021:5. 10.48550/arXiv.2107.10330.
[59] J. Jiang, T.B. Britton, A.J. Wilkinson, Evolution of dislocation density distributions in copper during tensile deformation, Acta Mater. 61 (2013) 7227–7239, https://doi.org/10.1016/J.ACTAMAT.2013.08.027.
[60] T.B. Britton, J.L.R.R. Hickey, Understanding deformation with high angular resolution electron backscatter diffraction (HR-EBSD), IOP Conf. Ser. Mater. Sci. Eng. 304 (2018), 012003, https://doi.org/10.1088/1757-899X/304/1/012003.
[61] S. Kalácska, Z. Dankházi, G. Zilahi, X. Maeder, J. Michler, P.D. Ispánovity, et al., Investigation of geometrically necessary dislocation structures in compressed Cu micropillars by 3-dimensional HR-EBSD, Mater. Sci. Eng. A 770 (2020), 138499, https://doi.org/10.1016/J.MSEA.2019.138499.
[62] D. Wallis, L.N. Hansen, B.T. Ben, A.J Wilkinson, Dislocation interactions in olivine revealed by HR-EBSD, J. Geophys. Res. Solid Earth 122 (2017) 7659–7678, https://doi.org/10.1002/2017JB014513.
[63] C. Moussa, M. Bernacki, R. Besnard, N. Bozzolo, About quantitative EBSD analysis of deformation and recovery substructures in pure Tantalum, IOP Conf. Ser. Mater. Sci. Eng. 89 (2015), 012038, https://doi.org/10.1088/1757-899X/89/1/012038.
[64] S.I. Wright, M.M. Nowell, EBSD image quality mapping, Microsc. Microanal. 12 (2006) 72–84, https://doi.org/10.1017/S1431927606060090.
[65] X. Tao, A. Eades, Alternatives to image quality (IQ) mapping in EBSD, Microsc. Microanal. 8 (2002) 692–693, https://doi.org/10.1017/S1431927602106465.
[66] M.J. McLean, W.A. Osborn, *In-situ* elastic strain mapping during micromechanical testing using EBSD, Ultramicroscopy 185 (2018) 21–26, https://doi.org/10.1016/J.ULTRAMIC.2017.11.007.
[67] Data Sheet Zeron® 100 (UNS S32760). Temperance, MI: 2000.
[68] A. Koko, E. Elmukashfi, T.H. Becker, P.S. Karamched, A.J. Wilkinson, T.J. Marrow, *In situ* characterisation of the strain fields of intragranular slip bands in ferrite by high-resolution electron backscatter diffraction, Acta Mater. 239 (2022), 118284, https://doi.org/10.1016/J.ACTAMAT.2022.118284.
[69] C. Örnek, M.G. Burke, T. Hashimoto, D.L. Engelberg, 748K (475°C) embrittlement of duplex stainless steel: effect on microstructure and fracture behavior, Metall. Mater. Trans. A 48 (2017) 1653–1665, https://doi.org/10.1007/s11661-016-3944-2.
[70] K.L. Weng, H.R. Chen, J.R. Yang, The low-temperature aging embrittlement in a 2205 duplex stainless steel, Mater. Sci. Eng. A 379 (2004) 119–132, https://doi.org/10.1016/J.MSEA.2003.12.051.
[71] H.J. Beattie, F.L. Versnyder, A new complex phase in a high-temperature alloy, Nature 178 (1956) 208–209, https://doi.org/10.1038/178208b0.
[72] Q. Zhang, A.S.S. Singaravelu, Y. Zhao, T. Jing, N. Chawla, Mechanical properties of a thermally-aged cast duplex stainless steel by nanoindentation and micropillar compression, Mater. Sci. Eng. A 743 (2019) 520–528, https://doi.org/10.1016/J.MSEA.2018.11.112.
[73] H.J. Lee, B.S. Kong, G.O. Subramanian, J. Heo, C. Jang, K.S Lee, Evaluation of thermal aging of δ-ferrite in austenitic stainless steel weld using nanopillar compression test, Scr. Mater. 155 (2018) 32–36, https://doi.org/10.1016/J.SCRIPTAMAT.2018.06.016.
[74] Z. Li, Y. Hu, T. Chen, X. Wang, P. Liu, Y. Lu, Microstructural evolution and mechanical behavior of thermally aged cast duplex stainless steel, Materials 13 (2020) 1–13, https://doi.org/10.3390/MA13245636 (Basel).
[75] Y. Fan, T.G. Liu, L. Xin, Y.M. Han, Y.H. Lu, T. Shoji, Thermal aging behaviors of duplex stainless steels used in nuclear power plant: a review, J. Nucl. Mater. 544 (2021), 152693, https://doi.org/10.1016/J.JNUCMAT.2020.152693.
[76] M.M. Nowell, R.A. Witt, B.W. True, EBSD Sample Preparation: techniques, tips, and tricks, Microsc. Today 13 (2005) 44–49, https://doi.org/10.1017/S1551929500053669.
[77] S. Jiapeng, L. Cheng, J. Han, A. Ma, L. Fang, Nanoindentation induced deformation and pop-in events in a silicon crystal: molecular dynamics simulation and experiment, Sci. Rep. 7 (2017) 10282, https://doi.org/10.1038/s41598-017-11130-2.
[78] J. Jiang, T.B. Britton, A.J. Wilkinson, Measurement of geometrically necessary dislocation density with high resolution electron backscatter diffraction: effects of detector binning and step size, Ultramicroscopy 125 (2013) 1–9, https://doi.org/10.1016/J.ULTRAMIC.2012.11.003.
[79] H. Abdolvand, A.J. Wilkinson, On the effects of reorientation and shear transfer during twin formation: comparison between high resolution electron backscatter diffraction experiments and a crystal plasticity finite element model, Int. J. Plast. 84 (2016) 160–182, https://doi.org/10.1016/J.IJPLAS.2016.05.006.
[80] T.B. Britton, J. Jiang, R. Clough, E. Tarleton, A.I. Kirkland, A.J. Wilkinson, Assessing the precision of strain measurements using electron backscatter diffraction – part 1: detector assessment, Ultramicroscopy 135 (2013) 126–135, https://doi.org/10.1016/j.ultramic.2013.08.005.
[81] T.B. Britton, A.J. Wilkinson, Measurement of residual elastic strain and lattice rotations with high resolution electron backscatter diffraction, Ultramicroscopy 111 (2011) 1395–1404, https://doi.org/10.1016/j.ultramic.2011.05.007.
[82] S.A. Kim, W.L. Johnson, Elastic constants and internal friction of martensitic steel, ferritic-pearlitic steel, and α-iron, Mater. Sci. Eng. A 452–453 (2007) 633–639, https://doi.org/10.1016/j.msea.2006.11.147.
[83] M.A. Hopcroft, W.D. Nix, T.W. Kenny, What is the Young's Modulus of Silicon? J. Microelectromech. Syst. 19 (2010) 229–238, https://doi.org/10.1109/JMEMS.2009.2039697.
[84] S.G. Lekhnitskii, General Equations of the Theory of Elasticity of an Anisotropic Body. Theory of Elasticity of an Anisotropic Elastic Body, 1st ed., MIR Publishers, Moscow, 1981, pp. 15–73.
[85] T.B. Britton, V.S. Tong, J. Hickey, A. Foden, A.J. Wilkinson, AstroEBSD : exploring new space in pattern indexing with methods launched from an astronomical approach, J. Appl. Crystallogr. 51 (2018) 1525–1534, https://doi.org/10.1107/S1600576718010373.
[86] T.B. Britton, J. Jiang, Y. Guo, A. Vilalta-Clemente, D. Wallis, L.N. Hansen, et al., Tutorial: crystal orientations and EBSD — or which way is up? Mater. Charact. 117 (2016) 113–126, https://doi.org/10.1016/j.matchar.2016.04.008.
[87] A. Koko, E. Elmukashfi, K. Dragnevski, A.J. Wilkinson, T.J. Marrow, J-integral analysis of the elastic strain fields of ferrite deformation twins using electron backscatter diffraction, Acta Mater. 218 (2021), 117203, https://doi.org/10.1016/j.actamat.2021.117203.
[88] W.H. Press, S.A. Teukolsky, W.T. Vetterling, B.P. Flannery, Numerical recipes in C. The Art of Scientific Computing, 2nd ed., Cambridge University Press, USA, 1992.
[89] A. Koko, T.H. Becker, E. Elmukashfi, N.M. Pugno, A.J. Wilkinson, T.J. Marrow, HR-EBSD analysis of *in situ* stable crack growth at the micron scale, J. Mech. Phys. Solids 172 (2023), 105173, https://doi.org/10.1016/j.jmps.2022.105173.
[90] S. Goel, N. Haque Faisal, X. Luo, J. Yan, A. Agrawal, Nanoindentation of polysilicon and single crystal silicon: molecular dynamics simulation and experimental validation, J. Phys. D Appl. Phys. 47 (2014), 275304, https://doi.org/10.1088/0022-3727/47/27/275304.
[91] H. Abdolvand, A.J. Wilkinson, Assessment of residual stress fields at deformation twin tips and the surrounding environments, Acta Mater. 105 (2016) 219–231, https://doi.org/10.1016/j.actamat.2015.11.036.
[92] T.B. Britton, J.L.R. Hickey, Understanding deformation with high angular resolution electron backscatter diffraction (HR-EBSD), IOP Conf. Ser. Mater. Sci. Eng. 304 (2018), 012003, https://doi.org/10.1088/1757-899X/304/1/012003.

[93] C. Zhu, K. Kaufmann, K.S. Vecchio, Novel remapping approach for HR-EBSD based on demons registration, Ultramicroscopy 208 (2020), 112851, https://doi.org/10.1016/J.ULTRAMIC.2019.112851.
[94] C. Zhao, X. Li, Quantitative study of residual strain and geometrically necessary dislocation density using HR-EBSD method, Exp. Mech. 61 (2021) 1281–1290, https://doi.org/10.1007/S11340-021-00741-6/FIGURES/14.
[95] J. Jiang, T.B. Britton, A.J. Wilkinson, Mapping type III intragranular residual stress distributions in deformed copper polycrystals, Acta Mater. 61 (2013) 5895–5904, https://doi.org/10.1016/J.ACTAMAT.2013.06.038.
[96] C. Kurniawan, C. Zhu, M. DeGraef, Deformation state extraction from electron backscatter diffraction patterns via simulation-based pattern-matching, Scr. Mater. 190 (2021) 147–152, https://doi.org/10.1016/J.SCRIPTAMAT.2020.09.004.
[97] R.R. Keller, A. Roshko, R.H. Geiss, K.A. Bertness, T.P. Quinn, EBSD measurement of strains in GaAs due to oxidation of buried AlGaAs layers, Microelectron. Eng. 75 (2004) 96–102, https://doi.org/10.1016/J.MEE.2003.11.010.
[98] S.I. Wright, M.M. Nowell, D.P. Field, A review of strain analysis using electron backscatter diffraction, Microsc. Microanal. 17 (2011) 316–329, https://doi.org/10.1017/S1431927611000055.
[99] R. Barabash, G. Ice, Strain and Dislocation Gradients from Diffraction, Imperial College Press, 2014, https://doi.org/10.1142/p897.